

Thermal Conductivity Comparison of Indium Gallium Zinc Oxide Thin Films: Dependence on Temperature, Crystallinity, and Porosity

Boya Cui,^{†,‡} Li Zeng,[†] Denis Keane,^{§,⊥} Michael J. Bedzyk,^{†,§} D. Bruce Buchholz,[§] Robert P. H. Chang,^{†,§} Xinge Yu,^{||} Jeremy Smith,^{||} Tobin J. Marks,^{||} Yu Xia,[#] Antonio F. Facchetti,^{||,#} Julia E. Medvedeva,[&] and M. Grayson^{*,†,‡}

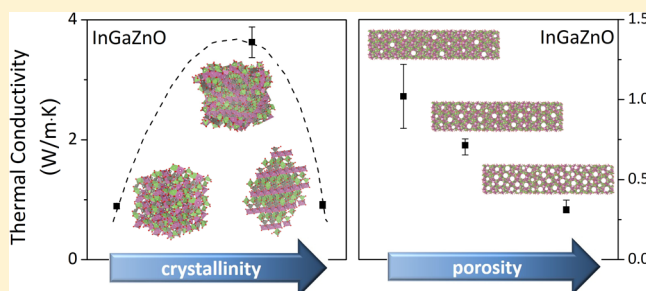
[†]Graduate Program in Applied Physics, [‡]Department of Electrical Engineering and Computer Science, [§]Department of Material Science and Engineering, and ^{||}Department of Chemistry, Northwestern University, Evanston, Illinois 60208, United States

[⊥]Northwestern Synchrotron Research Center, Argonne, Illinois 60439, United States

[#]Polyera Corporation, Skokie, Illinois 60077, United States

[&]Department of Physics, Missouri University of Science and Technology, Rolla, Missouri 65409, United States

ABSTRACT: The cross-plane thermal conductivity of InGaZnO (IGZO) thin films was measured using the 3ω technique from 18 to 300 K. The studied morphologies include amorphous (a-IGZO), semicrystalline (semi-c-IGZO), and *c*-axis-aligned single-crystal-like IGZO (c-IGZO) grown by pulsed laser deposition (PLD) as well as a-IGZO deposited by sputtering and by solution combustion processing. The atomic structures of the amorphous and crystalline films were simulated with *ab initio* molecular dynamics. The film quality and texturing information was assessed by X-ray diffraction and grazing incidence wide-angle X-ray scattering. X-ray reflectivity was also conducted to quantify film densities and porosities. All the high-density films exhibit an empirical power-law temperature dependence of the thermal conductivity $\kappa \sim T^{0.6}$ in the specified temperature range. Among the PLD dense films, semi-c-IGZO exhibits the highest thermal conductivity, remarkably exceeding both films with more order (c-IGZO) and with less order (a-IGZO) by a factor of 4. The less dense combustion-synthesized films, on the other hand, exhibited lower thermal conductivity, quantitatively consistent with a porous film using either an effective medium or percolation model. All samples are consistent with the porosity-adapted Cahill–Pohl (p-CP) model of minimum thermal conductivity.



1. INTRODUCTION

Indium gallium zinc oxide (IGZO) thin films have attracted scientific and technological attention due to their high carrier mobility, low intrinsic carrier concentration, good optical transparency, and consistent uniformity over large areas.^{1–5} These IGZO properties are useful for device applications^{6,7} such as display backplanes, smart windows, and low-cost flexible transparent electronics. Single-crystalline IGZO was first proposed to be a high-performance active channel material in transparent field-effect transistors since electron mobilities as high as $\mu \approx 80 \text{ cm}^2/(\text{V s})$ were reported.¹ Furthermore, amorphous phase a-IGZO is also useful for flexible electronics owing to the ability to process at room temperature⁸ and achieve mobilities $\mu > 10 \text{ cm}^2/(\text{V s})$ far exceeding that of amorphous silicon² (a-Si:H). Most studies have focused on characterizing and optimizing electrical and optical properties; however, a careful study of the thermal properties has been lacking. Such a study of IGZO thermal conductivity is useful for effective thermal management in IGZO devices, such as thin-film transistors in display backplanes. Knowledge of the thermal conductivity helps to model heat generation within that active layer and the thermal distribution throughout the device.⁹ Additionally, IGZO has

been proposed as a thermoelectric candidate, in a similar fashion to other transparent oxides such as¹⁰ InZnO. IGZO may have a competitive thermoelectric figure of merit¹¹ compared with other oxide materials, suggesting the intriguing possibility of “invisible thermoelectric devices” made with transparent oxides.^{12,13} Furthermore, the large-area capabilities might allow for integration into solar panels for photovoltaic/thermal hybrid systems¹⁴ to generate power from unavoidable waste heat. It might also act as the *n*-type layer of the recently proposed *p* × *n*-type transverse thermoelectrics¹⁵ for novel thermal management geometries. Moreover, an understanding of thermal transport in a-IGZO may yield clues to differentiate various fabrication methods, linking the thermal properties to the film structure and fabrication technique and eventually identifying strategies for improving electron mobility.

To our knowledge, there are only a few prior studies on IGZO thermal conductivity κ , and those were conducted at room temperature only. Seo et al.¹² studied the thermoelectric

Received: December 10, 2015

Revised: March 9, 2016

Published: March 9, 2016

performance of sputtered IGZO thin films and reported that remarkably the more ordered crystalline film has a factor of 7 lower thermal conductivity than the less ordered polycrystalline film. This counterintuitive variation of thermal conductivity on morphology begs confirmation as well as motivating a more detailed temperature-dependent study to achieve a better understanding of the underlying physics. Thermal conductivity for sputtered a-IGZO thin films¹⁶ was also reported, but again only at room temperature, thereby limiting the utility in comparing with theory.

This work will examine the temperature-dependent thermal conductivity of IGZO thin films fabricated with different techniques that are systematically analyzed and compared. Growth methods for comparison include pulsed laser deposition (PLD), sputtering, and spray-¹⁷ and spin-combustion⁸ solution processing. Among the PLD films, a series were grown under different conditions to vary the crystallinity, from amorphous (a-), to semicrystalline (semi-c-), to single-crystal-like (c-) phases. *Ab initio* molecular dynamics is also employed to determine the local structure of amorphous IGZO and to compare the room temperature atomic displacements in a- and c-IGZO. X-ray studies, including X-ray diffraction (XRD), grazing incidence wide-angle scattering (GIWAXS), and X-ray reflectivity (XRR), complement the thermal conductivity studies to assess the film density, porosity, crystallinity, and crystal orientation of the films processed by various means. The temperature-dependent thermal conductivity of IGZO thin films is characterized from 18 to 300 K using the 3ω technique.

Following the theoretical literature, we will adopt the term “vibrons”¹⁸ to refer to the generic vibrational modes responsible for thermal transport, since phonons represent relevant modes of heat propagation only in crystalline materials. We note that in all morphologies the heat is primarily conducted through vibrons rather than electrons, because even for highly doped IGZO films with electrical conductivity $\sigma = 100$ S/cm the electronic contribution to the thermal conductivity is only $\sigma_e = 7.3 \times 10^{-2}$ W/(m K) according to Wiedemann–Franz law—less than 10% of even the poorest thermally conducting PLD film. The electrical conductivity σ of IGZO can be tuned in a wide range⁶ ($\sigma = 10^{-3}$ – 10^2 S/cm) to target various applications, but all the films under study were grown to have relatively low $\sigma < 5 \times 10^{-1}$ S/cm to guarantee negligible electron contribution.

2. METHODS

2.1. Film Growth. Three different IGZO growth techniques were used: two physical deposition methods (PLD and sputtering) and one chemical synthesis method (combustion-based solution process). To facilitate thermal conductivity measurements, all films were grown on sapphire substrates for their high thermal conductivity.

We first discuss the PLD films. Film growth was carried out with a $\lambda = 248$ nm KrF excimer laser having a $\Delta t = 25$ ns pulse duration and operated at $f = 2$ Hz. InGaO₃(ZnO)₁ films of $d = 200$ nm thickness were grown by PLD from dense, hot-pressed targets (25 mm diameter). The $E = 200$ mJ/pulse beam was focused onto a 1.5 mm \times 2.5 mm spot size. The target was rotated at 5 rpm to prevent localized heating and fixed at 10 cm away from the substrates. The deposition oxygen ambient pressure for all films was 25 mTorr.

For PLD films, X-ray diffraction revealed how different substrate growth temperatures could induce morphologies from crystal-like to amorphous as well as an intermediate morphology exhibiting both crystalline and amorphous features (semicrystal-

line).¹⁹ Single-crystal-like InGaO₃(ZnO)₁ films (c-IGZO) were grown by first depositing a thin (5 nm) ZnO film at 700 °C from a ZnO target prior to the 200 nm thick IGZO film at 600 °C from an InGaO₃(ZnO)₂ target. The relatively low deposition temperature for the IGZO was used to prevent excessive loss of zinc. The film was then postannealed at 900 °C for 9 h. Semicrystalline InGaO₃(ZnO)₁ films (semi-c-IGZO) were grown by depositing an IGZO film directly on sapphire at 600 °C from an InGaO₃(ZnO)₂ target, followed by a postanneal at 600 °C for 6 h. During the anneal of c- and semi-c-IGZO, further loss of zinc is prevented by placing a blank sapphire substrate over the film, and the stoichiometry of InGaO₃(ZnO)₁ for the finished films was confirmed by the energy dispersive spectrum (EDS). The amorphous films were deposited by PLD at 25 °C; hence, the loss of zinc was relatively minor. Three targets were used to deposit the amorphous InGaO₃(ZnO)₁ films: InGaO₃(ZnO)₂, ZnO, and Ga₂O₃ targets. They are deposited in a cyclic fashion, 32 pulses InGaO₃(ZnO)₂, 4 pulses ZnO, 4 pulses Ga₂O₃; EDS confirms a stoichiometry of InGaO₃(ZnO)₁. Note: to deposit a monolayer of InGaO₃(ZnO)₂ would require an excess of 40 pulses; hence, the three constituents of the film described above are not stratified but mixed on a sub-unit-cell level. A computer-controlled shuttle was used to alternate ablation between targets. No postdeposition anneal was required for the amorphous films.

Sputtered a-IGZO films were grown by magnetron sputtering under an Ar and O₂ mixture (Ar:O₂ = 20 sccm:1 sccm, deposition pressure $P = 3 \times 10^{-3}$ Torr) using a target with In:Ga:Zn ratio of 1:1:1, to match the PLD stoichiometry. The films were annealed in air at 350 °C for 1 h after deposition, resulting in 50 nm thick films on sapphire substrates.

For solution-processed a-IGZO, both spray combustion synthesis¹⁷ and spin-coating combustion synthesis⁸ were used to deposit the films. Solutions were prepared with In(NO₃)₃· x H₂O, Zn(NO₃)₂· x H₂O, and Ga(NO₃)₃· x H₂O in 2-methoxyethanol to yield a 0.05 M metal concentration. Next, 55 μ L of NH₄OH and 100 μ L of acetylacetone were added into 10 mL of the metal nitrate solutions and stirred overnight at 25 °C. Prior to spray- or spin-coating, the precursor solutions were combined in the same molar ratio In:Ga:Zn = 1:1:1 and stirred for 2 h. For spray-coating, substrates were maintained at 300 °C on a hot plate while 0.05 M precursor solutions were loaded into the spray gun and sprayed intermittently (60 s cycles) onto sapphire substrates until the desired thickness (50 nm) was obtained. The nozzle–substrate distance was 20 cm. For multilayer 50 nm thick spin-coated devices, 0.05 M precursor solutions were spun at 3500 rpm for 30 s and then annealed for 10 min at 300 °C; this was repeated 15 times to achieve the desired thickness. For one-step 50 nm single-layer devices, precursor solutions with concentrations of 0.5 M were spin-coated at 2000 rpm for 60 s and then annealed for 30 min. All solution processed films were then postannealed at 300 °C for 1 h in clean dry air.

2.2. Device Processing and Measurements. Several processing steps were conducted on the films before the thermal conductivity measurements. An 80 nm thick SiN_x layer was deposited by plasma-enhanced chemical vapor deposition (PECVD) at 300 °C on all the samples to electrically isolate the IGZO films,⁴ followed by photolithographically patterned gold filaments deposited by thermal evaporation and lift-off. The gold filaments are typically 120–150 nm thick with a 10 nm chromium adhesion layer underneath.

The cross-plane thermal conductivity of IGZO thin films was obtained using the differential 3ω method,^{20,21} where the thermal signal is compared between samples with and without

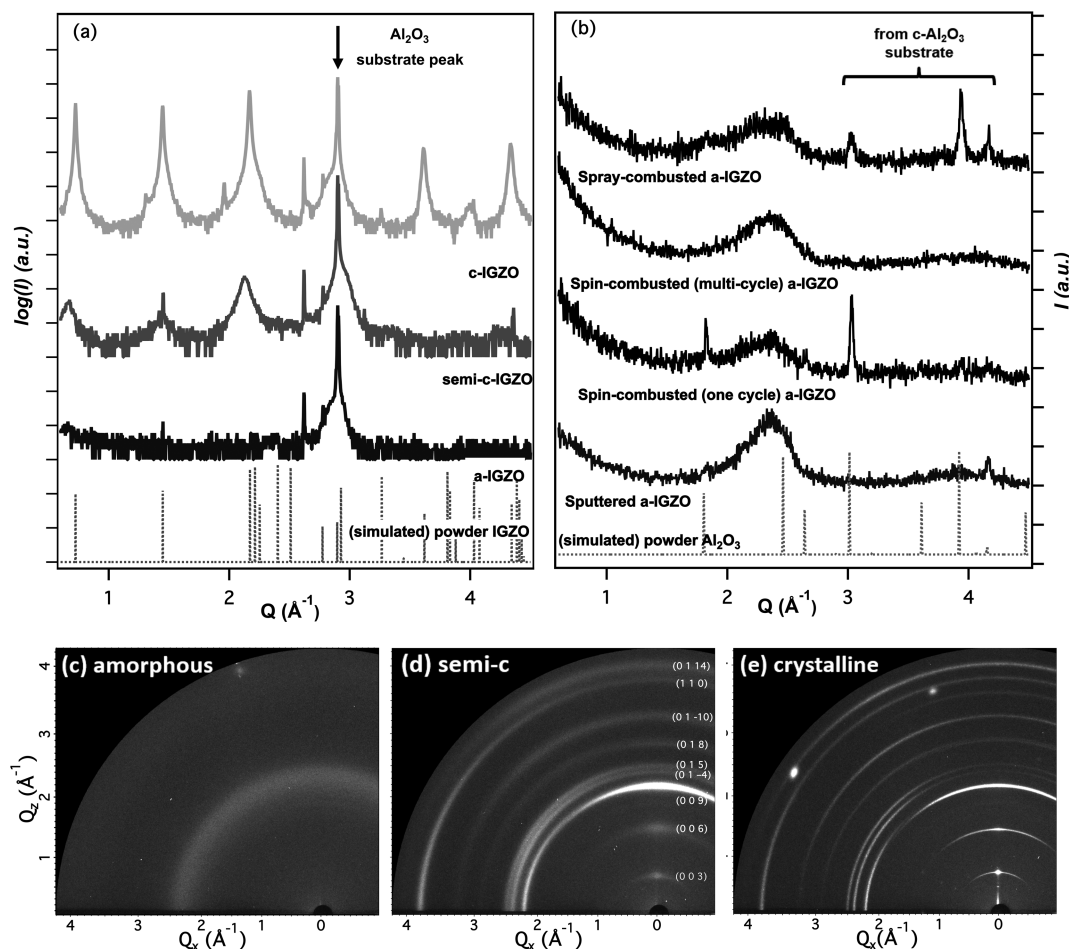


Figure 1. (a) XRD patterns of PLD-grown a-, semi-c-, and c-IGZO films. (b) GIWAXS study for sputtered and solution-processed a-IGZO. (c–e) Two-dimensional GIWAXS patterns of PLD-grown a-, semi-c-, and c-IGZO films, respectively, corresponding to those shown in (a).

the film of interest. The gold filaments act as both heater for ac current heating and thermometer for ac temperature oscillation measurement. The temperature coefficient of resistance for the filament, $(1/R)(dR/dT)$, is obtained during a slow cooldown, and the voltage oscillation, $V_{3\omega}$, is measured at a frequency of 3ω due to ac heating from an applied 1ω voltage $V_{1\omega}$. The temperature oscillation $T_{2\omega}$ at a frequency of 2ω can be deduced as

$$T_{2\omega} = 2 \frac{dT}{dR} \frac{R}{V_{1\omega}} V_{3\omega} \quad (1)$$

The temperature difference between the filaments with and without the underlying film $\Delta T_{2\omega,f}$ is the 2ω temperature difference across the IGZO film of interest, giving the film thermal conductivity as follows:²¹

$$\kappa_f = \frac{Pt}{2bl\Delta T_{2\omega,f}} \quad (2)$$

where P is the ac heating power, t is the thickness of the film, and l and b are the length and half-width of the filament, respectively. The width of the gold filament is $2b = 30 \mu\text{m}$, designed to be much larger than the thickness of the films ($t = 200 \text{ nm}$ for the PLD-grown films and $t = 50 \text{ nm}$ for the sputtered and solution-processed films) so the heat flow is predominantly in the vertical cross-plane direction. The completed devices were loaded into an Oxford variable temperature insert (VTI) helium gas flow

cryostat with coaxial shielded leads for temperature dependence study ranging from $T = 18$ to 300 K . Standard lock-in techniques were employed to extract the third harmonic term of the voltage across the filament relative to a dummy resistor with identical nominal resistance as the filament.

2.3. Ab Initio Molecular Dynamics Simulation. Molecular dynamics simulations were carried out to determine the atomic structure of a- and c-IGZO in order to better explain the thermal conductivity results. Amorphous InGaZnO structure was generated using first-principles molecular dynamics liquid-quench simulations as implemented in the Vienna Ab-initio Simulation Package (VASP).^{22–25} The calculations are based on density functional theory within generalized gradient approximation (GGA) with the PBE functional.²⁶ The initial cell $\text{In}_{18}\text{Ga}_{18}\text{Zn}_{18}\text{O}_{72}$ with rhombohedral structure and a density of $\rho = 6.33 \text{ g/cm}^3$ was melted at $T = 3000 \text{ K}$ for 6 ps to remove the crystalline memory; the melt was then rapidly quenched to $T = 100 \text{ K}$ at the rate of 200 K/ps . These simulated cooling rates are known from previous work¹⁹ to effectively match the coordination number of atoms in the simulated film to X-ray scattering data from experimental amorphous films grown at the substrate temperatures investigated here. During melting and quenching processes, a cutoff energy of $E = 260 \text{ eV}$ was used and the k-point sampling was restricted to Γ -point only. Finally, the structure was equilibrated at $T = 300 \text{ K}$ for 6 ps with a cutoff energy of $E = 300 \text{ eV}$. All simulations were carried out within NVT ensemble with Nosé–Hoover thermostat using integration

time step of 2 fs. The resulting atomic structures were plotted using VESTA software.²⁷ For crystalline InGaZnO₄, the experimental crystal structure was employed and the atomic coordinates were optimized using *ab initio* density functional calculations.²⁸

2.4. Modeling: Porosity-Adapted Cahill–Pohl (p-CP) Model. In quantitative comparison with the experimental data, we consider a simplified limit-case model proposed by Cahill and Pohl^{29,30} which predicts a lower bound or minimal thermal conductivity κ_{\min} . In the model, heat is transmitted by the random walk of damped and localized Einstein oscillators having different sizes and frequencies such that they follow the density of states of an acoustic phonon model. The generalized argument proposes that physically decoherent but coupled atoms cannot have a lower thermal conductivity than $\kappa_{\min}(T)$, with a wealth of experimental data on bulk materials and thin films cited therein to support this conclusion. The minimum thermal conductivity of an amorphous material is expressed as³⁰

$$\kappa_{\min}^{\text{CP}}(T) = \left(\frac{\pi}{6}\right)^{1/3} k_{\text{B}} n^{2/3} \sum_i v_i \left(\frac{T}{\Theta_i}\right)^2 \int_0^{\Theta_i/T} \frac{x^3 e^x}{(e^x - 1)^2} dx \quad (3)$$

where k_{B} is Boltzmann constant, n is the atom density per unit volume, v_i the speed of sound for each polarization i , and $\Theta_i = v_i(\hbar/k_{\text{B}})(6\pi^2 n)^{1/3}$, the Debye cutoff frequency expressed as a temperature. The sound velocity of two transverse modes (i.e., shear) v_s and one longitudinal mode (i.e., compression) v_c can be determined as^{31,32}

$$v_s = \sqrt{G/\rho_f}, \quad v_c = \sqrt{\left(K + \frac{4}{3}G\right)/\rho_f}$$

$$G = \frac{E}{2(1 + \nu)}, \quad K = \frac{E}{3(1 - 2\nu)} \quad (4)$$

where shear modulus G and bulk modulus K can be determined from Young's modulus E and Poisson's ratio ν .

Considering that all the films under study have different levels of porosity, the minimum thermal conductivity here has been adapted for porosity (p-CP model):

$$\kappa_{\min}(T) = f(P) \cdot \kappa_{\min}^{\text{CP}}(T) \quad (5)$$

where $f(P)$ is a porosity-adjusted factor that links the porous-film thermal conductivity κ to the dense counterpart κ_0 . This factor will be discussed further with two models in section 3.4.

3. RESULTS AND DISCUSSION

3.1. Morphology. Before the 3ω processing and measurement, the morphology of the three PLD samples with different crystallinities was examined both by XRD (Cu $K\alpha$, $\lambda = 1.54 \text{ \AA}$), as shown in Figure 1a, and by GIWAXS at the synchrotron (20 keV, $\lambda = 0.62 \text{ \AA}$) with a two-dimensional detector (MarCCD 165) as shown in Figure 1c–e. Since data were measured with different incident wavelengths, all figures were plotted as a function of Q ($= 4\pi \sin(\theta)/\lambda$) for comparison. The simulated IGZO and Al₂O₃ powder diffraction spectra were generated by CrystalMaker software based on crystal structural information obtained from inorganic crystal structure database (ICSD 247980 for IGZO and 10425 for Al₂O₃) with Cu $K\alpha$ wavelength as shown in (a) and (b) as dashed peaks, in order to determine the Miller indices and separate the substrate and film diffraction peaks, respectively.

The amorphous film grown by PLD shows no crystalline diffraction peaks in the XRD pattern in Figure 1a and presents an amorphous diffraction halo in the 2D GIWAXS image Figure 1c. For semi-*c*- and *c*-IGZO films, there are strong diffraction peaks in Figure 1a and diffraction rings in Figures 1d and 1e, respectively, which indicates semicrystalline structures and highly oriented features along the *c*-axis of the IGZO crystals in both films. The Miller indices of each diffraction peak were identified by matching with a simulated IGZO spectrum. Grain size analysis was performed by using the (009) diffraction peaks from the XRD data, and the grain size was determined to be $D = 6.9 \text{ nm}$ for the semi-*c* film and $D = 37.7 \text{ nm}$ for the *c*-IGZO film by applying the Scherrer equation.³³ This indicates that after annealing at 900 °C for 9 h *c*-IGZO has much a larger coherence length along the *c*-axis. Note that the measured grain size D above is still much smaller than the thickness of the PLD films $t = 200 \text{ nm}$; therefore, in the limit of $D \ll t$ vibrons are more likely to be scattered by grain boundaries rather than film–substrate interface, so we anticipate that interface effects will be negligible.

For samples grown by other methods (sputtering and combustion), the GIWAXS data (Cu $K\alpha$, $\lambda = 1.54 \text{ \AA}$) shown in Figure 1b indicate broad amorphous diffraction peaks ($Q = 2.36 \text{ \AA}^{-1}$) which confirm that the as-deposited films are amorphous. The difference between Figures 1a and 1b is that XRD patterns in (a) were taken under Bragg–Brentano geometry, while GIWAXS in (b) under grazing incident geometry. In GIWAXS setup by fixing incidence angle near the critical angle of IGZO thin film, the X-ray penetration depth is much shallower than the XRD result in (a), which explains why no intense (006) peak from the substrate near $Q = 2.90 \text{ \AA}^{-1}$ was seen in (b). A few crystalline diffraction peaks, for example peaks shown in $Q = 3\text{--}4.2 \text{ \AA}^{-1}$ for spray-combustion IGZO film, were observed in Figure 1b. These peaks match well with the simulated Al₂O₃ powder diffraction peaks shown as the gray trace at bottom of Figure 1b. Therefore, they most likely came from substrates when X-ray was projected on the edge of small sapphire substrate.

The X-ray reflectivity technique was used to extract the film electron density and convert it to mass density shown in Table 1,

Table 1. X-ray Reflectivity Results on the Density and Porosity of Films Fabricated by Physical Deposition (i.e., PLD³⁴ and Sputter) and Chemical Synthesis¹⁷ (i.e., Spray and Spin Combustion), in Order from Low to High Porosity

growth method	ρ_f (g/cm ³)	P (%)
PLD	6.12	4.4
sputter	5.86	8.4
spray	5.85	8.6
multicycle spin	5.09	20.5
single-cycle spin	3.82	40.0

based on the known stoichiometry (In:Ga:Zn:O = 1:1:1:4). The roughness root-mean-square is $\text{RMS} \approx 1 \text{ nm}$ for samples grown by PLD, and $\text{RMS} = 0.6 \text{ nm}$ for sputtered ones. All the solution-based combustion films have $\text{RMS} < 0.7 \text{ nm}$.¹⁷ We interpret the fraction of the reduced density as the porosity P , evaluated by comparing the film density ρ_f with the bulk density ρ_b :

$$P = 1 - \frac{\rho_f}{\rho_b} \quad (6)$$

The reference single crystal bulk density $\rho_b = 6.40 \text{ g/cm}^3$ was calculated from the ICSD database (#247980).

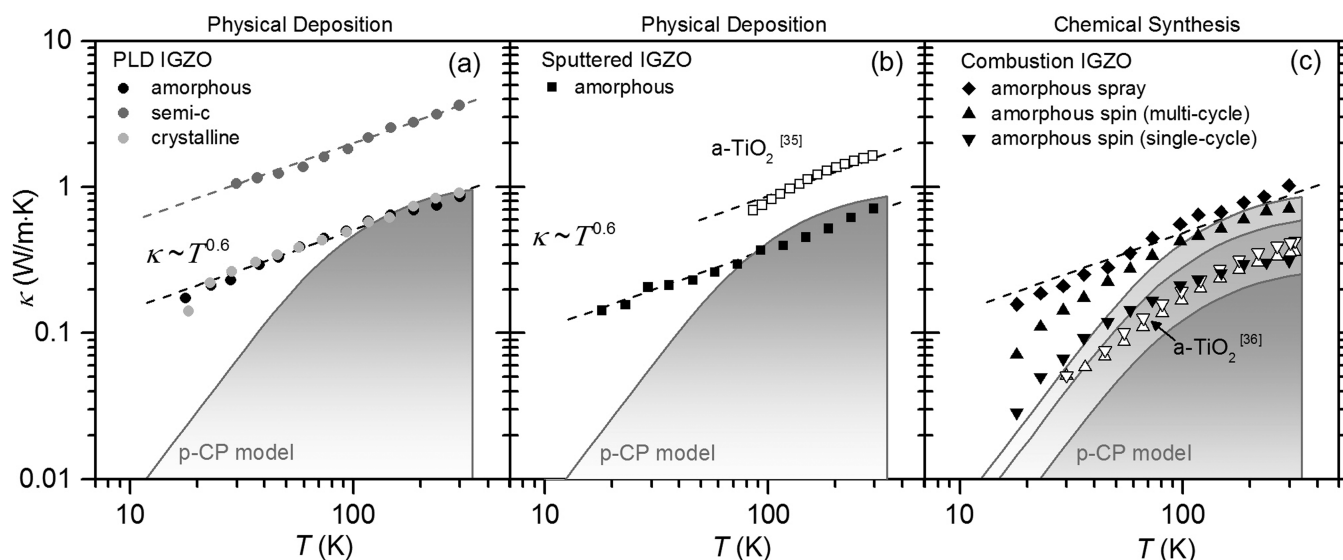


Figure 2. Temperature dependence of the thermal conductivity of all IGZO films under study, including (a) PLD films in different phases, (b) sputtered a-IGZO, and (c) combustion-processed a-IGZO. Comparison with another amorphous oxide^{35,36} a-TiO₂ is shown as open symbols in panel (b) for sputtered and panel (c) for sol-gel processed films. The dashed lines are guides to the eye showing the empirical power law of the temperature dependence $\kappa \sim T^{0.6}$ which holds over this temperature range. The gray areas are “forbidden”—below the theoretical minimum thermal conductivities based on the p-CP model (eq 5) where the porosity factor is adopted from the percolation theory (eq 8). In (c), the three p-CP curves correspond to the porosity of spray, multicycle, and single-cycle spin-combustion films respectively from the top to the bottom.

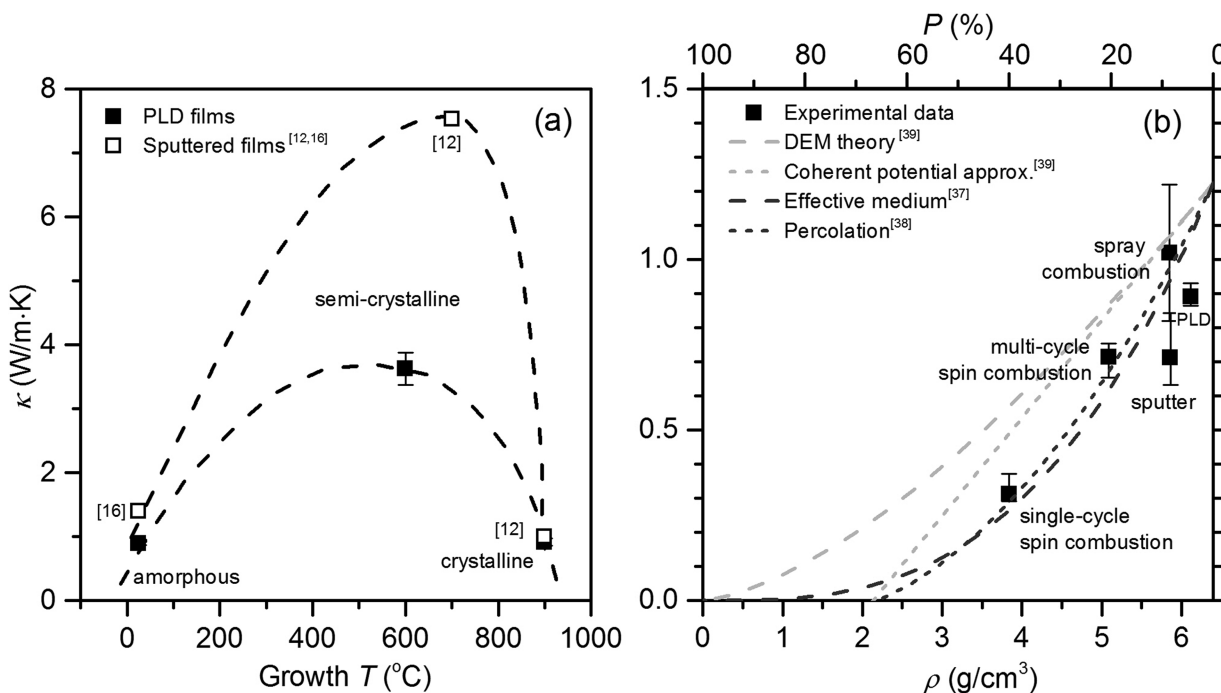


Figure 3. (a) Room-temperature thermal conductivity of a-, semi-c, and c-IGZO resulting from different substrate growth temperatures. The films from this work (filled squares) are PLD grown, and those of refs 12 and 16 (open squares) are sputtered. The dashed lines in (a) are guides to the eye. (b) Room-temperature thermal conductivity of a-IGZO films as a function of density (bottom x) or porosity (top x) caused by different growth methods. Best fits to the experimental data are shown with black dashed and dotted lines by an effective medium model by Gesele³⁷ et al. and a percolation model by Kirkpatrick,³⁸ respectively. For completeness, the lines in gray show two other models used for porous silica.³⁹ The representative error bars in both panels come from (1) the variation of $\Delta T_{2\omega,f}$ across the film in the frequency sweep (<10%) and (2) the variation of measured thermal conductivity with heating power (<15% for all samples⁴⁴). The temperature signal in 2ω across the IGZO layer is estimated to be about 10–15% of the total temperature drop through the sample (SiN_x/IGZO/sapphire substrate).

The density and porosity values of all the films are summarized in Table 1. The three PLD films with different morphologies are assumed to share the same high density and low porosity. On the other hand, the films grown by combustion show large variations

in porosity, where the multicycle spin-combustion film is almost 5 times as porous as the spray-combustion film, which itself has a density close to that of the physically deposited films. (Table 1). Given the hot substrate throughout the spray-combustion

process, one can expect spray-combustion films to trap very little of the gaseous combustion products (e.g., N_2 , CO_2 , and H_2O) in the material, yielding dense films similar to those fabricated by physical deposition.¹⁷ With spin-combustion, on the other hand, the substrate is cold upon deposition, and combustion takes place in a subsequent step. The single-cycle film is observed to have about half the porosity of multicycle film (Table 1). This is reasonable given that unlike the multicycle film which had an annealing process after each spin cycle, the single-cycle film has only one chance to release the gaseous products during the final annealing and consequently is prone to having a higher porosity, double that of the multicycle film.

3.2. Thermal Conductivity Summary. The results of the cross-plane 3ω thermal conductivity measurements on the different IGZO samples are summarized in Figure 2, where the different shades of the symbols in panel a represent different morphologies and the different symbol themselves refer to different growth methods across the panels a, b, and c. In Figure 2, all the physically deposited films (PLD-grown films in panel a and sputtered films in panel b) follow an empirical power law with temperature $\kappa \sim T^{0.6}$ from 18 K to room temperature, as shown by the dashed guiding lines. A prior measurement³⁵ on sputtered a-TiO₂, another transparent conducting oxide, also manifests the similar temperature dependence as shown in Figure 2b for comparison. For the three combustion processed a-IGZO samples in Figure 2c, the dense spray-combustion film exhibits the same temperature dependence $\kappa \sim T^{0.6}$ as the physically deposited IGZO films in Figure 2a, while the two porous spin-combustion a-IGZO films show deviations with reduced thermal conductivities at both the low-end and high-end temperatures relative to this power law. It should be noted that these latter two porous samples differ by a constant factor throughout the whole temperature range.

3.3. High-Density PLD Films: Role of Crystallinity. It is remarkable that all the three phases of PLD samples (a-, semi-c-, and c-IGZO) show the same power-law temperature dependence $\kappa \sim T^{0.6}$. Increasing temperatures should excite a broader spectrum of vibrons with different mean-free-path length scales. Although there is no obvious underlying cause for the similar temperature dependence of all three phases, their common power-law behavior suggests that all three phases have similar energy density of states and that they only differ by a common scaling factor for the mean-free path at all energies.

For PLD-grown IGZO films in Figure 2a, the a-IGZO almost perfectly overlaps the c-IGZO, both of which have a much lower thermal conductivity than that of semi-c-IGZO thin film. When the room-temperature behavior is plotted as a function of substrate temperature during deposition in Figure 3a, a striking nonmonotonic behavior emerges in the dependence of the thermal conductivity on crystalline order. A similar result was seen previously in room temperature experiments of sputtered IGZO films,^{12,16} also plotted in Figure 3a for comparison.

The intermediate-order semi-c-IGZO exhibited the highest thermal conductivity (Figures 2a and 3a). Crystalline and amorphous IGZO, on the other hand, show a relatively low and equal thermal conductivity. The atomic structures of all the three phases are illustrated in Figure 4, whereby panel a is a molecular dynamic simulation of the amorphous phase, panel c is the known superlattice-like structure of the crystalline phase, and panel b is schematically drawn to have intermediate order between these two extremes, representing the semicrystalline phase. The amorphous result is the easiest to explain, consistent with the strong scattering of vibration modes that one would

expect from the minimal short-range order in an amorphous structure⁴⁰ (Figure 4a). Crystalline *c*-axis aligned IGZO, however, is the most ordered film, yet its thermal conductivity is just as low as the amorphous film. This may be a result of the experiment measuring only out-of-plane *c*-axis thermal conductivity, and its superlattice-like structure with alternate stacking of In–O layers and Ga/Zn–O blocks⁴¹ in Figure 4c, creating regularly varying acoustic impedances. This is analogous to the thermal transport in superlattices^{42,43} and materials with planar defects perpendicular to *c*-axis,⁴⁴ where the stacking interfaces effectively act like scatterers and significantly suppress the cross-plane *c*-axis thermal conductivity. Finally, the other unexpected behavior is the significant *enhancement* of thermal conductivity for the semicrystalline phase. One would naively think that semicrystalline behavior would be an average of crystalline and amorphous, but a qualitatively different behavior is seen in the peak semi-c-IGZO conductance in Figure 3a. This work reproduces a similar result in refs 12 and 16 on sputtered IGZO films, also shown in Figure 3a. One explanation might be that individual grains have a large *a*–*b* plane conductivity^{45,46} which for half the grains is randomly oriented out-of-plane as illustrated in Figure 3b. Another explanation may be that grain boundary scattering dominates the reduced thermal conductivity of the crystalline state, and the medium range order of the semicrystalline state blurs the grain boundaries and allows crystalline regions to be continuously connected through an amorphous network. A future study of in-plane vs cross-plane thermal conductivity in crystalline IGZO would be able to distinguish these possible explanations but lies outside the scope of this present work.

3.4. Low-Density Spin-Combustion Films: Role of Porosity. Returning to Figure 2c, the thermal conductivity of the combustion processed films is examined to understand the role of porosity. To check the validity of these results, they can be compared to similarly processed films in the literature. Spin-combustion a-IGZO data are comparable to a-TiO₂ prepared by a sol–gel process³⁶ with porosity $P = 30\%$, since both are solution-processed and porous. The consistently low thermal conductivity appears correlated with their similarly high porosity. Note that the poor thermal conductivity of the porous a-IGZO films might seem attractive for thermoelectric applications, but in practice such materials would not serve this purpose because the electrical conductivity would also decrease significantly given the large porosity.

The thermal conductivities of the two spin-combustion films follow the same convex downward temperature dependence in Figure 2c and exhibit lower thermal conductivity compared with physically deposited dense films in Figure 2a,b. These two low-density films only differ by a constant factor throughout the entire temperature range in Figure 2c, and the proportionality factor can be explained by their different porosities. Gesele et al.³⁷ reported an effective medium model for porous Si and the following correlation between porosity and thermal conductivity:

$$f(P) = (1 - P)^3 \quad (7)$$

where κ_0 is the thermal conductivity of a dense bulk. In the limit of phonon mean free path l much smaller than pore size a , the phonon hydrodynamics model⁴⁷ takes pore size into consideration to arrive at this expression. Because of the amorphous nature of the thin film, the phonon mean free path of a-IGZO film can be quite short of order several atomic bonds, for example,¹⁶ $l = 0.35$ nm, which is much smaller than the typical

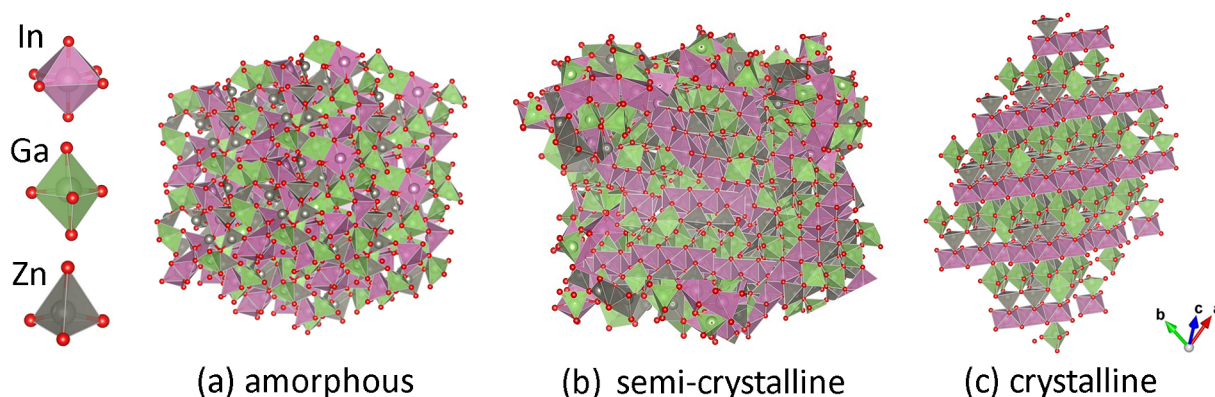


Figure 4. (a) Atomic structure of amorphous IGZO calculated from *ab initio* molecular dynamics liquid-quench simulations (b) Schematic representation of semi-c-IGZO, indicating more order than amorphous, but less order than crystalline. (c) Crystal structure of rhombohedral InGaZnO₄, where the Ga and Zn atoms are distributed randomly within the double layer. The small red spheres represent oxygen atoms, and cations are shown as polyhedra.

pore size¹⁷ $a = 2\text{--}3$ nm determined by positron annihilation spectroscopy for solution-processed porous films.

Alternatively to the effective medium model, percolation theory⁴⁸ can be adopted to explain the thermal conduction dependence on porosity, by regarding the porous a-IGZO film as a network of thermally conducting channels and insulating voids. Kirkpatrick³⁸ proposed the following reduction factor for conductivity in the percolation picture, in the low-porosity limit:^b

$$f(P) = [(1 - P) - 1.52P(1 - P)] \quad (8)$$

Both the effective medium and percolation models fit the room-temperature experimental results equally well, as is shown in Figure 3b. For the model calculation, $\kappa_0 = 1.23$ W/(m K) is assumed, which is the averaged dense-film thermal conductivity calibrated by single-cycle spin and PLD a-IGZO films using eq 7. Unlike the effective medium model, the percolation model has a threshold porosity $P_c = 65.8\%$, above which κ becomes vanishingly small since beyond this point the material only consists of isolated interpenetrating a-IGZO clusters with no covalently connected path for heat conduction.

There are other theories modeling the thermal conductivity in heterogeneous materials, for example, the differential effective medium (DEM) theory and coherent potential approximation⁴⁹ (Figure 3b). Compared with these theoretical predictions in gray, the a-IGZO system exhibits a more dramatically decreased thermal conductivity with increasing porosity. Although previous experimental results of thermal conductivity of porous silica matched these models well,³⁹ these other models are not able to capture the sharper decrease of thermal conductivity with porosity observed in our combustion processed films.

3.5. Comparison with P-CP Model. There have been many theoretical modelings of amorphous thermal conductivity. In the absence of a lattice, some theories describe generic thermal modes of vibration around equilibrium lattice positions in terms of vibrons, including propagating modes (propagons) and nonpropagating modes (fractons).¹⁸ Although linear temperature dependence $\kappa \sim T$ is commonly observed^{50,51} and explained with resonant scattering⁵² or phonon-assisted fracton hopping,⁵³ a large amount of work shows deviations^{21,54,55} from this linear behavior, including the present study. Jagannathan et al.⁵⁶ proposed that the strong anharmonic coupling of phonon and fracton can quench the fracton hopping rate and lead to slower rise of κ with increasing T . Then several lattice-dynamics-

based numerical calculations were conducted,^{57,58} including the contribution from nonpropagating vibrational states. More recently, a Green–Kubo mode analysis⁵⁹ was developed taking anharmonic atomic interactions into consideration.

Given this diversity of theories, we therefore chose to compare the data to a porosity-adjusted Cahill–Pohl model discussed in section 2.4 due to the simplicity and universality of this theory. The p-CP curves for different a-IGZO are plotted as an upper boundary of the gray areas in Figures 2a–c. Note that in the low T limit the integral in eq 3 yields a constant, leading to the temperature dependence $\kappa \sim T^2$, seen as an asymptotic power-law slope on the left of the log–log plot. On the other hand, in the high T limit, κ approaches a constant, as seen on the right of the p-CP curves. The porosity factor $f(P)$ in the p-CP model (eq 5) is adopted from the percolation theory (eq 8) due to its better fit with our experimental data (Figure 3b). For calculating $\kappa_{\min}^{\text{CP}}(T)$, $E = 130$ GPa is taken from a past report¹⁶ on IGZO. Poisson’s ratio ν does not vary much among thin films: For example, $\nu = 0.33\text{--}0.42$ for a-Si:H films,⁶⁰ $0.25\text{--}0.4$ for a-C:H films,⁶⁰ 0.3 for a-SiN_x films,⁶¹ and 0.27 for poly-c-SiN_x films.⁶² So in the absence of direct measurement of Poisson’s ratio for IGZO, we use that of another transparent conducting oxide ITO thin film⁶³ $\nu = 0.35$.

Figures 2a and 2b show consistency with the p-CP model in that the measured thermal conductivities remain at or above the model value. Below 30 K, the data exceed the κ_{\min} value by half an order of magnitude. Whereas the CP model assumes that the lifetime of all vibrational modes is half an oscillation period, the observed difference at low T between the measured data and the CP model shows that the longer-wavelength modes must be significantly longer-lived than half an oscillation period.

For combustion processed films, the p-CP model fits the increasingly porous films remarkably well (Figure 2c), correctly predicting the low- and high-temperature deviations below the empirical $\kappa \sim T^{0.6}$ fit. In this regard, it appears that porous films serve as exemplary Cahill–Pohl minimal thermal conductors, provided that the correct porosity factor $f(P)$ is identified for scaling the CP model. The percolation model³⁸ for $f(P)$ gives the best fit curves shown here.

4. CONCLUSIONS

The temperature dependence of cross-plane thermal conductivity of InGaZnO films is measured with the 3ω method from 18 to 300 K, including films grown by various techniques (PLD,

sputtering, spray- and spin-combustion) and with different crystalline structures (amorphous, semicrystalline, and single-crystal-like IGZO for PLD films). X-ray techniques XRD, GIWAXS, and XRR were conducted to obtain the film morphologies, including crystal orientation, crystallinity, density, and porosity.

All the dense films follow the same empirical power law $\kappa \sim T^{0.6}$, while the two low-density films by combustion exhibit a concave downward temperature dependence which fits very well with a porosity-adjusted Cahill–Pohl model. Among all the dense PLD films in different morphologies, semi-c-IGZO was found to have the highest thermal conductivity, even higher than that of more ordered c-IGZO. The low thermal conductivities of a-IGZO and c-IGZO films are attributed to the strong scattering in the short-range order and stacking of atom layer interfaces, respectively. For semi-c-IGZO, an anisotropic thermal conductivity for individual randomly oriented grains could possibly explain the increased cross-plane thermal conductivity observed, as could a blurring of grain boundaries in the semi-c phase. These models could be distinguished by conducting in-plane and cross-plane thermal conductivity measurements in future work. The atomic structures of different phases were obtained from *ab initio* molecular dynamics. The low-density films show considerably smaller thermal conductivity compared with the dense ones. Applying the effective medium model and percolation model, one can explain the reduced thermal conductivity of these porous films throughout the whole temperature range as a function of their porosities.

The results above will provide important information for the thermal management of IGZO-based devices and figure-of-merit estimates of IGZO as thermoelectrics, and bring new fundamental understanding to transport in amorphous porous materials.

AUTHOR INFORMATION

Corresponding Author

*E-mail: m-grayson@northwestern.edu (M.G.).

Notes

The authors declare no competing financial interest.

ACKNOWLEDGMENTS

This work was supported by the NSF MRSEC program DMR-1121262 at Materials Research Science and Engineering Center of Northwestern University. We utilized Northwestern University Micro/Nano Fabrication Facility (NUFAB) and the EPIC facility (NUANCE Center-Northwestern University) which has received support from the MRSEC program NSF DMR-1121262 at the Materials Research Center; the International Institute for Nanotechnology (IIN); and the State of Illinois, through the IIN. This work also made use of the J.B. Cohen X-ray Diffraction Facility supported by the NSF-MRSEC program DMR-1121262. GIWAXS measurement was carried out at the 5BMC beamline of the DuPont–Northwestern–DOW Collaboration Assess Team (DND-CAT) at the Advanced Photon Source (APS) at Argonne National Laboratory (ANL). B.C. also thanks Jiajun Luo for electrical measurement of the samples and useful discussion.

ADDITIONAL NOTES

^aFor all the samples the leakage resistance between the filament and substrate exceeded 1 G Ω , except for the spray-combustion film ($R \sim 0.5$ M Ω), whose behavior was consistent with other

films of comparable density. So we include this data for completeness but with larger error bars in Figure 3b, arising from the power dependence of the thermal conductivity.

^bThis expression was shown to be valid for porosities up to 40%.³⁸

REFERENCES

- (1) Nomura, K.; Ohta, H.; Ueda, K.; Kamiya, T.; Hirano, M.; Hosono, H. Thin-film transistor fabricated in single-crystalline transparent oxide semiconductor. *Science* **2003**, *300*, 1269–1272.
- (2) Nomura, K.; Ohta, H.; Takagi, A.; Kamiya, T.; Hirano, M.; Hosono, H. Room-temperature fabrication of transparent flexible thin-film transistors using amorphous oxide semiconductors. *Nature* **2004**, *432*, 488–492.
- (3) Nomura, K.; Takagi, A.; Kamiya, T.; Ohta, H.; Hirano, M.; Hosono, H. Amorphous oxide semiconductors for high-performance flexible thin-film transistors. *Jpn. J. Appl. Phys.* **2006**, *45*, 4303.
- (4) Yabuta, H.; Sano, M.; Abe, K.; Aiba, T.; Den, T.; Kumomi, H.; Nomura, K.; Kamiya, T.; Hosono, H. High-mobility thin-film transistor with amorphous InGaZnO₄ channel fabricated by room temperature rf-magnetron sputtering. *Appl. Phys. Lett.* **2006**, *89*, 112123.
- (5) Kim, M.; Jeong, J. H.; Lee, H. J.; Ahn, T. K.; Shin, H. S.; Park, J.-S.; Jeong, J. K.; Mo, Y.-G.; Kim, H. D. High mobility bottom gate InGaZnO thin film transistors with SiO_x etch stopper. *Appl. Phys. Lett.* **2007**, *90*, 212114.
- (6) Hosono, H. Ionic amorphous oxide semiconductors: Material design, carrier transport, and device application. *J. Non-Cryst. Solids* **2006**, *352*, 851–858.
- (7) Kamiya, T.; Nomura, K.; Hosono, H. Present status of amorphous In-Ga-Zn-O thin-film transistors. *Sci. Technol. Adv. Mater.* **2010**, *11*, 044305.
- (8) Kim, M.-G.; Kanatzidis, M. G.; Facchetti, A.; Marks, T. J. Low-temperature fabrication of high-performance metal oxide thin-film electronics via combustion processing. *Nat. Mater.* **2011**, *10*, 382–388.
- (9) Hsieh, T.-Y.; Chang, T.-C.; Chen, T.-C.; Tsai, M.-Y.; Chen, Y.-T.; Chung, Y.-C.; Ting, H.-C.; Chen, C.-Y. Origin of self-heating effect induced asymmetrical degradation behavior in InGaZnO thin-film transistors. *Appl. Phys. Lett.* **2012**, *100*, 232101.
- (10) Ohta, H.; Seo, W.-S.; Koumoto, K. Thermoelectric properties of homologous compounds in ZnO–In₂O₃ system. *J. Am. Ceram. Soc.* **1996**, *79*, 2193–2196.
- (11) Williams, D. S. Thermoelectric properties of a-IGZO. Ph.D. Thesis, State University of New York at Binghamton, 2013.
- (12) Seo, D. K.; Shin, S.; Cho, H. H.; Kong, B. H.; Whang, D. M.; Cho, H. K. Drastic improvement of oxide thermoelectric performance using thermal and plasma treatments of the InGaZnO thin films grown by sputtering. *Acta Mater.* **2011**, *59*, 6743–6750.
- (13) Kim, J. H.; Seo, D. K.; Ahn, C. H.; Shin, S. W.; Cho, H. H.; Cho, H. K. Hybrid solution processed InGaO₃(ZnO)_m thin films with periodic layered structures and thermoelectric properties. *J. Mater. Chem.* **2012**, *22*, 16312–16317.
- (14) Chávez-Urbiola, E.; Vorobiev, Y. V.; Bulat, L. Solar hybrid systems with thermoelectric generators. *Sol. Energy* **2012**, *86*, 369–378.
- (15) Zhou, C.; Birner, T.; Tang, Y.; Heinselman, K.; Grayson, M. Driving Perpendicular Heat Flow: ($p \times n$)-Type Transverse Thermoelectrics for Microscale and Cryogenic Peltier Cooling. *Phys. Rev. Lett.* **2013**, *110*, 227701.
- (16) Yoshikawa, T.; Yagi, T.; Oka, N.; Jia, J.; Yamashita, Y.; Hattori, K.; Seino, Y.; Taketoshi, N.; Baba, T.; Shigesato, Y. Thermal conductivity of amorphous indium gallium zinc oxide thin films. *Appl. Phys. Express* **2013**, *6*, 021101.
- (17) Yu, X.; Smith, J.; Zhou, N.; Zeng, L.; Guo, P.; Xia, Y.; Alvarez, A.; Aghion, S.; Lin, H.; Yu, J.; et al. Spray-combustion synthesis: Efficient solution route to high-performance oxide transistors. *Proc. Natl. Acad. Sci. U. S. A.* **2015**, *112*, 3217–3222.
- (18) Fabian, J.; Allen, P. B. Anharmonic decay of vibrational states in amorphous silicon. *Phys. Rev. Lett.* **1996**, *77*, 3839.

- (19) Buchholz, D. B.; Ma, Q.; Alducin, D.; Ponce, A.; Jose-Yacamán, M.; Khanal, R.; Medvedeva, J. E.; Chang, R. P. The structure and properties of amorphous Indium Oxide. *Chem. Mater.* **2014**, *26*, 5401–5411.
- (20) Cahill, D. G. Thermal conductivity measurement from 30 to 750 K: 3ω method. *Rev. Sci. Instrum.* **1990**, *61*, 802–808.
- (21) Cahill, D. G.; Katiyar, M.; Abelson, J. R. Thermal conductivity of a-Si:H thin films. *Phys. Rev. B: Condens. Matter Mater. Phys.* **1994**, *50*, 6077–6082.
- (22) Kresse, G.; Hafner, J. Ab initio molecular dynamics for liquid metals. *Phys. Rev. B: Condens. Matter Mater. Phys.* **1993**, *47*, 558.
- (23) Kresse, G.; Hafner, J. Ab initio molecular-dynamics simulation of the liquid-metal-amorphous-semiconductor transition in germanium. *Phys. Rev. B: Condens. Matter Mater. Phys.* **1994**, *49*, 14251.
- (24) Kresse, G.; Furthmüller, J. Efficient iterative schemes for ab initio total-energy calculations using a plane-wave basis set. *Phys. Rev. B: Condens. Matter Mater. Phys.* **1996**, *54*, 11169.
- (25) Kresse, G.; Furthmüller, J. Efficiency of ab-initio total energy calculations for metals and semiconductors using a plane-wave basis set. *Comput. Mater. Sci.* **1996**, *6*, 15–50.
- (26) Perdew, J. P.; Burke, K.; Ernzerhof, M. Generalized gradient approximation made simple. *Phys. Rev. Lett.* **1996**, *77*, 3865.
- (27) Momma, K.; Izumi, F. VESTA 3 for three-dimensional visualization of crystal, volumetric and morphology data. *J. Appl. Crystallogr.* **2011**, *44*, 1272–1276.
- (28) Murat, A.; Adler, A. U.; Mason, T. O.; Medvedeva, J. E. Carrier generation in multicomponent wide-bandgap oxides: InGaZnO₄. *J. Am. Chem. Soc.* **2013**, *135*, 5685–5692.
- (29) Cahill, D. G.; Pohl, R. O. Lattice vibrations and heat transport in crystals and glasses. *Annu. Rev. Phys. Chem.* **1988**, *39*, 93–121.
- (30) Cahill, D. G.; Pohl, R. O. Heat flow and lattice vibrations in glasses. *Solid State Commun.* **1989**, *70*, 927–930.
- (31) Kinsler, L. E.; Frey, A. R.; Coppens, A. B.; Sanders, J. V. *Fundamentals of Acoustics*, 4th ed.; Wiley: 1999.
- (32) Sokolnikoff, I. S.; Specht, R. D. *Mathematical Theory of Elasticity*; McGraw-Hill: 1956; Vol. 83.
- (33) Scherrer, P. Bestimmung der Grösse und der inneren Struktur von Kolloidteilchen mittels Röntgenstrahlen. *Nachr. Ges. Wiss. Göttingen, Math.-Phys. Kl.* **1918**, *1918*, 98–100.
- (34) Adler, A. U. Defect analysis of the In-Ga-Zn-O system for transparent oxide semiconductor applications. Ph.D. Thesis, Northwestern University, 2013.
- (35) Cahill, D. G.; Allen, T. H. Thermal conductivity of sputtered and evaporated SiO₂ and TiO₂ optical coatings. *Appl. Phys. Lett.* **1994**, *65*, 309–311.
- (36) Fang, J.; Reitz, C.; Brezesinski, T.; Nemanick, E. J.; Kang, C. B.; Tolbert, S. H.; Pilon, L. Thermal conductivity of highly-ordered mesoporous titania thin films from 30 to 320K. *J. Phys. Chem. C* **2011**, *115*, 14606–14614.
- (37) Gesele, G.; Linsmeier, J.; Drach, V.; Fricke, J.; Arens-Fischer, R. Temperature-dependent thermal conductivity of porous silicon. *J. Phys. D: Appl. Phys.* **1997**, *30*, 2911.
- (38) Kirkpatrick, S. Percolation and conduction. *Rev. Mod. Phys.* **1973**, *45*, 574.
- (39) Costescu, R. M.; Bullen, A. J.; Matamis, G.; O'Hara, K. E.; Cahill, D. G. Thermal conductivity and sound velocities of hydrogen-silsesquioxane low-k dielectrics. *Phys. Rev. B: Condens. Matter Mater. Phys.* **2002**, *65*, 094205.
- (40) Kittel, C. Interpretation of the thermal conductivity of glasses. *Phys. Rev.* **1949**, *75*, 972–974.
- (41) Li, C.; Bando, Y.; Nakamura, M.; Onoda, M.; Kimizuka, N. Modulated structures of homologous compounds InMO₃(ZnO)_m (M = In, Ga; m = Integer) described by four-dimensional superspace group. *J. Solid State Chem.* **1998**, *139*, 347–355.
- (42) Chen, G. Thermal conductivity and ballistic-phonon transport in the cross-plane direction of superlattices. *Phys. Rev. B: Condens. Matter Mater. Phys.* **1998**, *57*, 14958.
- (43) Venkatasubramanian, R. Lattice thermal conductivity reduction and phonon localizationlike behavior in superlattice structures. *Phys. Rev. B: Condens. Matter Mater. Phys.* **2000**, *61*, 3091.
- (44) Brooks, C. M.; Wilson, R. B.; Schäfer, A.; Mundy, J. A.; Holtz, M. E.; Muller, D. A.; Schubert, J.; Cahill, D. G.; Schlom, D. G. Tuning thermal conductivity in homoepitaxial SrTiO₃ films via defects. *Appl. Phys. Lett.* **2015**, *107*, 051902.
- (45) Yang, B.; Liu, W.; Liu, J.; Wang, K.; Chen, G. Measurements of anisotropic thermoelectric properties in superlattices. *Appl. Phys. Lett.* **2002**, *81*, 3588–3590.
- (46) Zhou, C.; Cui, B.; Vurgaftman, I.; Canedy, C.; Kim, C.; Kim, M.; Bewley, W.; Merritt, C.; Abell, J.; Meyer, J.; et al. Thermal conductivity tensors of the cladding and active layers of interband cascade lasers. *Appl. Phys. Lett.* **2014**, *105*, 261905.
- (47) Alvarez, F.; Jou, D.; Sellitto, A. Pore-size dependence of the thermal conductivity of porous silicon: a phonon hydrodynamic approach. *Appl. Phys. Lett.* **2010**, *97*, 033103.
- (48) Stauffer, D.; Aharony, A. *Introduction to Percolation Theory*; CRC Press: 1994.
- (49) Bruggeman, V. D. Berechnung verschiedener physikalischer Konstanten von heterogenen Substanzen. I. Dielektrizitätskonstanten und Leitfähigkeiten der Mischkörper aus isotropen Substanzen. *Ann. Phys.* **1935**, *416*, 636–664.
- (50) de Oliveira, J.; Page, J.; Rosenberg, H. Heat transport by fracton hopping in amorphous materials. *Phys. Rev. Lett.* **1989**, *62*, 780.
- (51) Choy, C.; Tong, K.; Wong, H.; Leung, W. Thermal conductivity of amorphous alloys above room temperature. *J. Appl. Phys.* **1991**, *70*, 4919–4925.
- (52) Karpov, V.; Parshin, D. On the thermal conductivity of glasses at temperatures below the Debye temperature. *Zh. Eksp. Teor. Fiz.* **1985**, *88*, 2212–2227.
- (53) Alexander, S.; Entin-Wohlman, O.; Orbach, R. Phonon-fracton anharmonic interactions: The thermal conductivity of amorphous materials. *Phys. Rev. B: Condens. Matter Mater. Phys.* **1986**, *34*, 2726.
- (54) Cahill, D. G.; Pohl, R. O. Thermal conductivity of amorphous solids above the plateau. *Phys. Rev. B: Condens. Matter Mater. Phys.* **1987**, *35*, 4067.
- (55) Zink, B.; Pietri, R.; Hellman, F. Thermal conductivity and specific heat of thin-film amorphous silicon. *Phys. Rev. Lett.* **2006**, *96*, 055902.
- (56) Jagannathan, A.; Orbach, R.; Entin-Wohlman, O. Thermal conductivity of amorphous materials above the plateau. *Phys. Rev. B: Condens. Matter Mater. Phys.* **1989**, *39*, 13465.
- (57) Feldman, J. L.; Kluge, M. D.; Allen, P. B.; Wooten, F. Thermal conductivity and localization in glasses: Numerical study of a model of amorphous silicon. *Phys. Rev. B: Condens. Matter Mater. Phys.* **1993**, *48*, 12589.
- (58) Allen, P. B.; Feldman, J. L.; Jaroslav, F.; Frederick, W. Anharmonic decay of vibrational states in amorphous silicon. *Philos. Mag. B* **1999**, *79*, 1715.
- (59) Lv, W.; Henry, A. Direct calculation of modal contributions to thermal conductivity via Green–Kubo modal analysis. *New J. Phys.* **2016**, *18*, 013028.
- (60) Jiang, X.; Reichelt, K.; Stritzker, B. The hardness and Young's modulus of amorphous hydrogenated carbon and silicon films measured with an ultraload indenter. *J. Appl. Phys.* **1989**, *66*, 5805–5808.
- (61) Taylor, J. A. The mechanical properties and microstructure of plasma enhanced chemical vapor deposited silicon nitride thin films. *J. Vac. Sci. Technol., A* **1991**, *9*, 2464–2468.
- (62) Lynch, C. T. *Practical Handbook of Materials Science*; CRC Press: 1989.
- (63) Neerincq, D.; Vink, T. Depth profiling of thin ITO films by grazing incidence X-ray diffraction. *Thin Solid Films* **1996**, *278*, 12–17.